Coupled full waveform inversion of horizontal borehole ground penetrating radar data to estimate soil hydraulic parameters: A synthetic study

Yi Yu[1,2], Johan Alexander Huisman[1], Anja Klotzsche[1,2], Harry Vereecken[1,2] and Lutz Weihermüller[1]

[1]Agrosphere (IBG-3), Institute of Bio- and Geosciences, Forschungszentrum Jülich GmbH, 52425 Jülich, Germany

[2]HPSC TerrSys, Centre for High-Performance Scientific Computing in Terrestrial Systems, Geoverbund ABC/J, Jülich, Germany

Corresponding author: Yi Yu, email: y.yu@fz-juelich.de

1. Introduction

Accurate estimation of soil hydraulic parameters is crucial for the reliable prediction of water flow and solute transport in the vadose zone, which is the foundation for studying many environmentally relevant processes such as ground water recharge (e.g., Gómez-Hernández and Gorelick, 1989; Peleg and Gvirtzman, 2010; Pollacco et al., 2008) and actual evaporation (e.g., Diouf et al., 2020; Doble et al., 2016). Ground penetrating radar (GPR) is one of the most widely used geophysical techniques to address water-related issues (e.g., Bano, 2006; Bradford, 2008; Doolittle et al., 2006). GPR uses the propagation of high frequency electromagnetic waves in the subsurface to investigate the soil bulk dielectric permittivity and the soil electrical conductivity (Daniels, 2005). Although, the soil hydraulic parameters cannot be directly measured by GPR, time-lapse GPR measurements can be used to determine soil water content (SWC) dynamics (e.g., Huisman et al., 2003; Klotzsche et al., 2018) that are directly influenced by soil hydraulic properties because of the strong link between SWC and bulk dielectric permittivity (Topp et al., 1980). In the last decades, significant progress has been made with the use of different GPR configurations (surface, off-ground, and borehole GPR) to estimate soil hydraulic parameters (e.g., Busch et al., 2013, Jadoon et al., 2008; Jadoon et al., 2012; Lambot et al., 2006, Kowalsky et al., 2004, Rossi et al., 2015, Rucker and Ferré, 2004, Yu et al., 2021). Borehole GPR has a larger investigation depth and a better control of the vertical resolution than off-ground and surface GPR (Huisman et al., 2003), and thus shows advantages for estimating soil hydraulic parameters, especially at specialized test sites with appropriate boreholes (e.g., Binley et al., 2001; Looms et al., 2008; Kowalsky et al., 2005).

Borehole GPR data are conventionally processed by using ray-based inversion approaches (e.g., Irving et al., 2007), which only provide velocity and attenuation information obtained from the first arrival times and first cycle amplitudes of the GPR data, respectively. Such ray-based approaches generally have a limited resolution for subsurface characterization because only a small amount of the data is considered. Therefore, ray-based inversions have difficulty to provide information resolving small-scale high-contrast layers, such as high-porosity zones that could be related to preferential flow zones in aquifer systems or impermeable clay lenses (Klotzsche et al., 2019a). In contrast, full-waveform inversion (FWI) of GPR data considers the entire measured signal, including reflections and refractions, and is therefore able to provide more accurate and spatially higher resolved permittivity and electrical conductivity information than ray-based methods. The FWI method was first proposed by Tarantola (1984) for seismic data. FWI of seismic data has been further developed since then and is currently widely used (e.g., Berkhout, 2012; Brossier et al., 2009; Vigh and Starr, 2008). A comprehensive overview of FWI developments and applications is provided by Virieux and Operto (2009). Because of the similarity between seismic and GPR data, FWI has also been used for analyzing off-ground (e.g., Lambot and Andre, 2014), surface (e.g., Busch et al., 2014), and borehole GPR data (e.g., Ernst et al. 2007a; Ernst et al., 2007b; Meles et al., 2010; Klotzsche et al., 2013; Klotzsche et al., 2019a) to obtain high-resolution information on the spatial distribution of both dielectric permittivity and electric conductivity. The application of FWI for off-ground and surface GPR has mainly focused on estimating the properties of simplified models with a limited number of unknowns, such as layered media (Busch et al., 2012; Ihamouten et al., 2019) or cylindrical objects (Liu et al., 2018) in the subsurface. In contrast, FWI of vertical borehole GPR multi-offset gathers (MOG)

72 measurements can obtain high-resolution 2D subsurface images by using a gradient-based
73 inversion algorithm (e.g., Gueting et al., 2017; Klotzsche et al., 2010; Klotzsche et al.,
74 2014; Looms et al., 2017). GPR is also commonly conducted with horizontal boreholes
75 using zero-offset profiling (ZOP) measurements to estimate the distribution of dielectric
76 permittivity at specific depths (e.g., Galagedara et al., 2002). However, it is currently not
77 possible to employ the 2D gradient-based inversion algorithm for the FWI for horizontal
78 borehole ZOP data, because ZOP measurements do not provide the necessary dense ray-
79 coverage with a high amount of different ray-path angles. Additionally with the current
80 2D approach, we cannot account for the air-soil interfaces that cause significant
81 reflections and refractions of the waves. Until now, only a preliminary study was
82 performed by Klotzsche et al. (2016) to invert dielectric permittivity and electric
83 conductivity for a 2-layer soil profile from ZOP data using a shuffle complex evolution
84 approach (SCE-UA) (Duan et al., 1993). This approach worked well with synthetic GPR
85 data to retrieve the soil permittivity and conductivity, but is still challenging to apply to
86 measured GPR data, because it is difficult to estimate an effective source wavelet from a
87 single ZOP trace.
88
89 To estimate soil hydraulic properties from time-lapse geophysical data, many recent
90 studies have relied on a coupled inversion approach (e.g., Hinnell et al., 2010; Huisman
91 et al., 2010; Lambot et al., 2006; Mboh et al., 2012). Compared to a traditional sequential
92 inversion approach, where the hydrological model is inverted with SWC information
93 estimated from geophysical data, coupled inversion is recognized as a more reliable and
94 advanced approach that directly assimilates the geophysical data, and therefore, avoids
95 interpretation errors from data processing. Coupled inversion was applied successfully to

GPR travel times to estimate the soil hydraulic parameters at the field scale (Looms et al., 2008; Scholer et al., 2013; Yu et al., 2021). Since GPR waveforms are expected to contain more information about the subsurface than GPR travel times, it is anticipated that the combined use of coupled inversion and FWI (i.e., coupled full waveform inversion, CFWI) is potentially able to provide soil hydraulic parameter estimates with less uncertainty. Up to now, there are only a few studies that have reported the use of CFWI to estimate hydraulic parameters from time-lapse off-ground GPR measurements (Lambot et al., 2009) or synthetic seismic data (Li et al., 2020). However, no studies have been reported that applied CFWI to borehole GPR data for parameterizing hydrological models.

This study aims to investigate potential benefits and shortcomings of a coupled full-waveform inversion (CFWI) for estimating soil hydraulic parameters and layer thickness for a 2-layer profile using synthetic horizontal borehole GPR data. First, a workflow of the CFWI will be proposed. Next, a synthetic infiltration experiment will be designed to simulate SWC and GPR data and parameter correlations between hydraulic parameters and layer thickness will be analyzed for CFWI. Finally, CFWI will be applied to the synthetic data and the inversion results will be compared with the results from the more established coupled inversion of GPR travel times.

2 Materials and Methods

2.1 Horizontal borehole GPR measurements

ZOP measurements can be used to monitor SWC dynamics at the depths where boreholes were installed (e.g., Klotzsche et al., 2019b). To perform a ZOP survey, the transmitter and receiver antennas are moved simultaneously with the same spacing in two different

boreholes. Using a straight-wave approximation, the first arrival times from the ZOP survey can be used to determine a 1D dielectric profile using:

$$\varepsilon^{obs} = \left[\frac{c*\left(t^{obs}-T_0\right)}{d}\right]^2 \quad , \tag{1}$$

where ε^{obs} (-) is the observed dielectric permittivity, d (m) is the distance between two boreholes, t^{obs} (ns) is the first arrival time, c is the velocity of electromagnetic wave in vacuum (0.3 m ns^{-1}), and T_0 (ns) is the time-zero offset. This offset is commonly determined by conducting wide angle reflection and refraction (WARR) measurements with the borehole antennas in air. With respect to the details for obtaining T_0 from measured ZOP data, we refer to Klotzsche et al. (2019b). In the case of synthetic GPR data, T_0 commonly can be set manually. After obtaining the soil dielectric permittivity, SWC (θ^{obs}) can be calculated using the complex refractive index model (CRIM) (Roth et al., 1990):

$$\theta^{obs} = \frac{\sqrt{\varepsilon^{obs}}-(1-\Phi)\sqrt{\varepsilon_s}-\Phi}{\sqrt{\varepsilon_w}-1}, \tag{2}$$

where ε_s is the dielectric permittivity of the soil matrix (4.7 in this study), Φ is the soil porosity, and ε_w is the permittivity of water (84 at 10°C).

2.2 Hydrological and GPR forward modelling

The 1D vertical water flow in porous media can be described by the Richards equation:

$$\frac{\partial\theta(h)}{\partial t} = \frac{\partial}{\partial z}\left[K_r(h)\left(\frac{\partial h}{\partial z}+1\right)\right], \tag{3}$$

where $\theta(h)$ is the water retention function describing the relationship between the volumetric SWC (θ) (cm^3 cm^{-3}) and pressure head (h) (cm), $K_r(h)$ is the hydraulic conductivity (cm min^{-1}) as a function of the pressure head (h), t is time (min), z is the elevation coordinate (cm). $\theta(h)$ and $K_r(h)$ can be parameterized by the classical Mualem

143 - van Genuchten (MvG) model (Mualem, 1976; van Genuchten, 1980) as:

144 $$\theta(h) = \begin{cases} \theta_r + \frac{\theta_s - \theta_r}{(1+|\alpha h|^n)^m} & , h < 0 \\ \theta_s & , h \geq 0 \end{cases} , \quad (4)$$

145 $$K_r(h) = K_s S_e^l [1 - (1 - S_e^{1/m})^m]^2 , \quad (5)$$

146 with

147 $$S_e = \frac{\theta - \theta_r}{\theta_s - \theta_r} , \quad (6)$$

148 where θ_r and θ_s are the residual and saturated SWC (cm^3 cm^{-3}), respectively, α (cm^{-1})
149 and n (-) are empirical parameters that account for the inverse of the air-entry pressure
150 and the pore-size distribution, respectively, m (-) is classically related to n by $m = 1 - \frac{1}{n}$,
151 K_s (cm min^{-1}) is the saturated hydraulic conductivity, l (-) is an empirical parameter that
152 represents pore tortuosity and commonly set to 0.5 (van Genuchten, 1980), but can be
153 different for individual soils (Shinomiya et al., 2001), and S_e (-) is the effective saturation.
154 Using these constitutive relations, the soil hydraulic properties can be described with six
155 parameters (θ_r, θ_s, α, n, K_s, l).
156
157 For hydrological and GPR forward modelling, we used the approach already reported by
158 Yu et al. (2021). We only provide a short summary here. Hydrus-1D (Šimůnek et al.,
159 2008) was used to simulate the vertical soil water content dynamics. The total simulation
160 domain was 1.5 m deep and discretized with 151 nodes with an equal spacing of 1 cm. It
161 is assumed that the infiltration events were conducted on the bare soil and therefore the
162 root water uptake was neglected. Also, evaporation was not considered in the
163 hydrological modelling, because the evaporation rate was much lower than the infiltration
164 rate. An atmospheric boundary condition with surface run-off was used as the upper
165 boundary condition and a seepage face ($h = 0$) was used as the lower boundary condition.

166

167 gprMax3D (Giannopoulos, 2005; Warren et al., 2016) was used to simulate GPR wave
168 propagation using a finite-difference time-domain (FDTD) numerical method. In this
169 study, the size of the simulation domain for gprMax3D was set to 2 x 1.5 x 1.5 m,
170 including a soil profile of 0.8 m thickness. The absorbing boundary of the simulation
171 domain uses the perfectly matched layer (PML) approach. The node spacing of the
172 discretized FDTD grid was 0.02 m. We used a current source to excite the electromagnetic
173 waves. The center frequency of the current source was 200 MHz and the excitation
174 function was the first derivative of a Gaussian wavelet.

175

176 *2.3 Set-up of the coupled full waveform inversion*

177 We consider two inversion strategies in this study: coupled inversion of GPR travel
178 times (Fig. 1a) and coupled full waveform inversion (Fig. 1b). In both approaches,
179 vertical SWC profiles (θ^{mod}) were firstly obtained by Hydrus-1D simulation with
180 hydraulic parameters. And then, the dielectric permittivity profiles (ε^{mod}) used as input
181 for the gprMax3D simulations to obtain synthetic GPR data can be calculated from the
182 θ^{mod} by rearranging Eq. 2:

183 $$\varepsilon^{mod} = [(\sqrt{\varepsilon_w} - 1) * \theta^{mod} + (1 - \Phi) * \sqrt{\varepsilon_s} + \Phi]^2 \quad . \tag{7}$$

184 Finally, the measured GPR data will be optimized with synthetic GPR data to estimate
185 the hydraulic parameters. The main difference between CFWI and coupled inversion of
186 travel times is that CFWI directly minimizes the misfit between measured E^{obs} (V m^{-1})
187 and simulated waveforms E^{mod} (V m^{-1}) in the time domain instead of the misfit between
188 first arrival times. For the coupled inversion of travel times, it was assumed that the effects
189 of the soil electrical conductivity could be neglected, which is reasonable given that the

first arrival time is not sensitive to the soil electrical conductivity. In contrast, the soil electrical conductivity should be considered for GPR modelling in CFWI, since the soil electrical conductivity influences the attenuation, and thus, the amplitude of the GPR waveform. The distribution of the electrical conductivity can be reasonably obtained from the distribution of SWC and a petrophysical relationship, e.g., by Archie's law (Archie, 1942):

$$\sigma^{mod} = \frac{1}{k_a}\,\sigma_w \Phi^{m_a}\left(\frac{\theta^{mod}}{\Phi}\right)^{n_a}, \tag{8}$$

where σ^{mod} (S m^{-1}) is the bulk soil electrical conductivity used for GPR modelling, σ_w is the electrical conductivity of the water (assumed to be 0.0519 S m^{-1} here), k_a (-) is a tortuosity constant, n_a (-) is the saturation exponent and m_a (-) is the cementation exponent. In this study, k_a, n_a and m_a are assumed to 1, 2 and 2, respectively, as suggested by Ewing and Hunt (2005).

The cost function $C_{MVG}(t)$ (ns) for the coupled inversion of GPR travel times is the RMSE of modelled (t^{mod}) and observed (t^{obs}) GPR first arrival times:

$$C_{MVG}(t) = \sqrt{\frac{\sum_{i=1}^{n_t}(t_i^{mod} - t_i^{obs})^2}{n_t}}, \tag{9}$$

where n_t (-) is the number of GPR measurements. Similarly, the cost function $C_{MVG}(E)$ (V m^{-1}) for CFWI uses the RMSE between the modelled and measured electrical fields:

$$C_{MVG}(E) = \sqrt{\frac{\sum_{i=1}^{n_e}(E_i^{mod} - E_i^{obs})^2}{n_e}}, \tag{10}$$

where n_e (-) is the number of the electric field points in the modelled GPR data. It should be noted that the temporal sampling of simulated GPR waveforms is commonly higher than of measured GPR waveforms. To ensure that the measured and modelled data are of the same size, the measured GPR data need be interpolated to be the same

size of the synthetic GPR data.

In this study, the cost function for CFWI and coupled inversion of GPR travel times were minimized using SCE-UA (Duan et al., 1993), which is a general-purpose global optimization algorithm. The inversion was assumed to be converged if the cost-function value decreased to a specified value or the improvement of the best model was below 0.01 % in the last 10 evolution loops.

.4 Set-up for synthetic infiltration experiment

A synthetic case study is used to investigate the feasibility of obtaining plausible hydraulic parameter estimates for a 2-layer profile by using CFWI. The results of CFWI will be compared to results obtained with coupled inversion of GPR travel times as a reference. In this study, we employed a 2-layer soil profile to generate synthetic SWC profiles (Table 1) based on the hydraulic parameterization described by Cai et al. (2018) to represent the Selhausen test site (Germany). In this model, we changed the saturated hydraulic conductivity of the subsoil from 0.0004 cm min^{-1} reported by Cai et al. (2018) to 0.04 cm min^{-1}, because it should be greater than the infiltration rate to avoid ponding of water at the layer interface.

In the synthetic study, we considered a single 6-hour infiltration event (360 min) followed by a 90-min period with soil water redistribution without infiltration (Fig. 2a). The infiltration rate was 0.03 cm min^{-1}. Horizontal borehole GPR data were simulated at 0.2, 0.4, and 0.6 m depths every 30 min. The distance between transmitter and receiver antennas was 0.75 m.

The vertical SWC profiles at times when GPR measurements were conducted are shown in Fig. 2b. It can be seen, that the infiltration front reached the layer boundary at a depth of 0.3 m after 180 min. At the end of the infiltration event (360 min), the upper 0.6 m of soil was saturated and the infiltration front moved to 0.8 m depth. After the infiltration stopped, the infiltration front still moved down to a depth of 0.9 m and the SWC above 0.6 m depth slightly decreased due to redistribution. The synthetic time-lapse SWC data at 0.2, 0.4, and 0.6 m depths are shown in Fig. 3a. The soil at 0.2 and 0.4 m depth reached saturation after 200 and 300 min, respectively.

After obtaining the synthetic SWC profiles, the dielectric permittivity profiles used for GPR modelling were obtained using Eq. 7 and the electrical conductivity profiles were obtained using Eq. 8. These dielectric permittivity and electrical conductivity profiles were employed to generate synthetic GPR data with gprMax3D, which were then used to determine the GPR first arrival time data (Fig. 3b) by means of the automatic picking approach reported by Yu et al. (2021). A comparison of Fig. 3a and Fig. 3b shows that the synthetic time-lapse SWC data and GPR travel time data have synchronous dynamics during the entire experiment.

The GPR waveforms simulated before (0 min), at the beginning (30 min), middle (210 min), and end (420 min) of the infiltration event are shown in Fig. 3c for different borehole depths. In general, the waveforms simulated at different times show large differences, which was not always the case for the SWC measurements and the first arrival times. For example, the arrival time of the direct wave simulated at a 0.6 m depth

261 did not show a clear difference between 0 and 30 min (Fig. 3b), but the simulated GPR
262 waveforms are obviously different at these two measurement times (Fig. 3c). Moreover,
263 it is clear that the arrival times and waveforms of the reflected waves generated on the
264 air-soil boundary are different at these measurement times (see the waveforms between
265 12 ns and 15 ns in Fig. 3c). To explain this in detail, the wavefield snapshots for the GPR
266 measurements at 0.6 m depth were obtained at the infiltration times of 0 and 30 min (Fig.
267 4). At the early stage of the wave propagation (8 ns), only the direct waves can be
268 observed (Fig. 4a and 4b). As the infiltration front did reach the 0.6 m depth, the
269 waveforms of the direct wave that were measured by the receiver between 8 and 14 ns
270 (Fig. 3c) did not show differences at these two measurement times. The reflected waves
271 were generated on the soil surface at around 12 ns (Fig. 4b and 4c). Since the infiltration
272 event increased the SWC of the top 0.1 m of the soil at 30 min (see Fig. 2b), the
273 permittivity of the top soil and the reflection coefficient of the soil surface were changed.
274 As a result, the travel time and amplitude of the reflected waves measured by the receiver
275 between 15 and 20 ns (Fig. 3c) showed substantial differences (see Fig. 4e – 4h) at these
276 measurement times. The reflected wave simulated at 30 min showed later arrival times,
277 but have larger amplitude than that simulated at 0 min.
278
279 For a more realistic synthetic modelling study, Gaussian noise with zero mean and a
280 standard deviation of 0.1 ns (Δt) was added to the noise-free GPR travel time. The noise
281 level of 0.1 ns is based on the sampling interval of 0.2 ns typically used in horizontal
282 borehole GPR applications, which limits the accuracy of travel time determination. The
283 noise added to the GPR waveform data was based on noise evaluation using previously
284 measured GPR waveforms reported by Yu et al. (2020) at recorded times before the first

arrival, which showed that noise varied from 0.1 to 0.5% of the maximum amplitude. Therefore, Gaussian noise with zero mean and a standard deviation of 0.5% of the maximum amplitude (ΔE) was added to the simulated GPR waveforms in this synthetic study.

Before conducting the inversions, the response surface method (Vrugt and Dane, 2006) was employed to show the parameter uncertainty and correlation for CFWI and the coupled inversion of travel times by using a 2D grid search of the cost function distribution. As a reference, the response surface was also generated based on noisy SWC data that could be obtained by point measurements, such as time domain reflectometry (TDR). The noise level for SWC was assumed to be 0.01 $cm^3\ cm^{-3}$ (Topp and Ferré, 2005). The response surfaces for point measurements were generated based on the following cost function：

$$C_{MVG}(\theta) = \sqrt{\frac{\sum_{i=1}^{n_\theta}(\theta_i^{mod} - \theta_i^{obs})^2}{n_\theta}}\ , \tag{11}$$

where θ_i^{mod} and θ_i^{obs} are modelled and measured SWC, respectively, and n_θ(-) is the number of the point measurements.

Since no GPR measurements were generated in the dry condition during the infiltration experiment, the inversion will not be sensitive to the residual SWC (θ_r). Therefore, we intend to invert hydraulic parameters θ_s, α, n, K_s and the soil layer thickness (h_t) for a 2-layer soil profile. K_s will be inverted in its log-transform ($\log(K_s)$). After obtaining the final inversion results from CFWI and coupled inversion of GPR travel times, the uncertainty and the correlation coefficients between the estimated parameters were

evaluated using a first-order uncertainty approximation (Kool and Parker, 1988). Here, it was assumed that correlation coefficients that exceed 0.6 indicate an undesirably strong correlation.

3. Results

3.1 Response surfaces

In a first step, parameter correlations were analyzed using response surface analysis. Given the available computing power, it was not possible to calculate the response surface for all parameter pairs for a 2-layer profile in the case of GPR travel time and waveform data. Since no studies have reported the correlation between the layer thickness and hydraulic parameters until now, response surfaces considered in this study were specifically analyzed to reveal the correlations between layer thickness and different hydraulic parameters for a 2-layer soil profile from GPR waveforms, GPR travel times and true SWC data (Fig. 5).

In general, response surfaces obtained from different types of data showed similar parameter correlations. In the response surfaces for $h_t - n_1$ and $h_t - n_2$, a steep gradient of the cost function was observed near the global minimum, which indicates that h_t, n_1, and n_2 are well constrained by the inversion. However, in the response surfaces for $h_t - \log(K_{s1})$, $h_t - \log(K_{s2})$, $h_t - \alpha_1$, and $h_t - \alpha_2$ the misfit distribution was perpendicular to the h_t axis, suggesting that $\log(K_{s1})$, $\log(K_{s2})$, α_1, and α_2 are less well constrained in the inversion. The global minima in the response surfaces for $h_t - \theta_{s1}$ and $h_t - \theta_{s2}$ were positioned in an elongated valley, which implies that θ_{s1} and θ_{s2} are negatively correlated with h_t.

The misfit distributions in the response surfaces from SWC showed a strong change at h_t = 0.2 m and h_t = 0.4 m (Fig. 5), which were the depths where SWC data were simulated. To explain this, synthetic SWC data (Fig. 6a) were simulated by using h_t = 0.18 m and h_t = 0.22 m while keeping the other parameters at the optimal values (see blue crosses in Fig. 5a). Large SWC differences were observed at 0.2 m depth after the soil got fully saturated, because the saturated SWC at this depth was different for the models with h_t = 0.18 m and h_t = 0.22 m (θ_{s1}= 0.229 and θ_{s2} = 0.326 $cm^3\ cm^{-3}$). Similarly, models with the layer boundary below 0.4 m depth will also have different saturated SWCs. The response surfaces for GPR travel times and waveforms did not show a sudden change at h_t = 0.2 m and h_t = 0.4 m. Although, the simulations with h_t = 0.18 m and h = 0.22 m showed differences in GPR travel time (Fig. 6b) and GPR waveforms (Fig. 6c), the cost function values for GPR travel times (0.36 and 0.23 ns) and GPR waveforms (0.98 and 0.84 V m^{-1}) showed much less pronounced differences as the values for SWC (0.05 and 0.014 $cm^3\ cm^{-3}$). This can be explained by the fact that 200 MHz GPR measurements have a larger sampling volume than point measurements (Klotzsche et al., 2019b). Because of the spatial averaging, GPR travel times and waveforms will be less sensitive to abrupt changes in the vertical SWC profile.

Besides potential parameter correlations, it is also interesting to analyze normalized cost function values for different types of data to obtain qualitative insights in parameter uncertainty. The response surfaces show that many model parameters can be inverted with low uncertainty for the GPR waveform data (at least in theory) as indicated by the small area with a normalized error smaller than 1. To further illustrate this, two sets of

356 model parameters (black crosses in Fig. 5a) were selected in the response surfaces for
357 $h_t - \theta_{s1}$, while the other parameters were set to the optimal parameters. The temporal
358 dynamics in SWC, travel times, and waveforms were simulated for both sets of model
359 parameters (Fig. 7). Time series of SWC and travel time (Fig. 7a and 7b) only showed
360 very minor differences for these two sets of simulations. For the simulated GPR
361 waveforms (Fig. 7c), the two sets of model parameters also provide almost identical GPR
362 waveforms at the beginning of the experiment (30 min) because the infiltration front was
363 still located at a shallow depth in the first layer (Fig. 2b). When the infiltration front
364 approached the layer boundary (210 min), obvious differences appeared between the
365 waveforms from the true model and the two selected parameter sets, especially at the 0.2
366 m depth. To explain this in detail, wavefield snapshots were simulated with the true model
367 and the selected parameter sets (Fig. 8). Due the considerable SWC (permittivity)
368 differences between the first and second layer, a strong reflected wave was generated on
369 the layer boundary. Theoretically, a potential refracted wave was also generated on the
370 air-soil boundary, nevertheless, the energy of the refracted wave was very weak and
371 therefore its influence on first arrival time and waveform could be neglected. The
372 reflected wave was superimposed with the direct wave, but this did not affect the first
373 arrival time (Fig. 8a, 8b and 8c). Hence, the GPR travel times for the selected parameter
374 sets only showed minor differences. However, the path length and reflection coefficient
375 of the reflected wave are related to h_t, and thus, the travel time and amplitude of this
376 reflected wave were different. This resulted in substantial differences for the simulated
377 GPR waveforms (Fig. 8d and 8e) and explained the difference in GPR waveforms for
378 these models at the end of the infiltration (420 min). This analysis highlights that the
379 inversion of SWC and GPR travel times only contains information about the SWC at or

near the borehole depth. On the other hand, CFWI contains additional information on the SWC at other depths as well as the layer depth due to the reflected wave generated from the layer boundary. Therefore, CFWI is expected to outperform the inversion of SWCs and travel times for estimating hydraulic parameters and h_t.

3.2 Coupled inversion results

Hydraulic parameters were estimated by using coupled inversion of noisy travel times and waveforms (Table 2). To avoid overfitting, inversions were stopped when the noise levels for travel time (0.1 ns) and waveform data (0.03 V m^{-1}) were reached. In general, the noisy travel times (Fig. 9a) and waveforms (Fig. 9b) were fitted well by the estimated parameters. It was found that the waveforms simulated with the results of the coupled inversion of travel times resulted in a slight mismatch for several measurements, e.g., the measurement conducted at 0.2 m depth at 210 min. This is attributed to the fact that the coupled inversion of travel times did not use all the information contained in the waveforms. In the case of the coupled inversion of travel times, the inversely estimated parameters showed larger uncertainty than for CFWI especially for θ_{s1}, α_1, θ_{s2}, α_2, and h_t. The estimated values of n_1, $\log(K_{s1})$, n_2, and $\log(K_{s2})$ for CFWI still showed a slight deviation from the known reference values. This is likely caused by the correlations between $n_1 - \log(K_{s1})$ and $n_2 - \log(K_{s2})$. Other parameter combinations did not show strong correlations.

Fig. 10 presents 50 realizations of the water retention and relative hydraulic conductivity functions based on the estimated parameters from CFWI and coupled inversion of travel times and the associated uncertainty in Table. 2. Since the CFWI accurately obtained the hydraulic parameters with considerably smaller uncertainty, a very good match was found

405 between the estimated and true water retention and relative hydraulic conductivity
406 functions. However, for the coupled inversion of travel times, the estimated water
407 retention functions (Fig. 10a and 10c) showed relatively larger uncertainty and did not
408 accurately predict the true function at low pressure heads, because the n_1 and n_2 of the
409 true model were not within the uncertainty bounds of the estimated n_1 and n_2. In addition,
410 since the uncertainty interval of estimated K_{s2} did contain the true K_{s2} value, a slight
411 mismatch (Fig. 10d) of the estimated and true relative hydraulic conductivity functions
412 can be found when the second layer is close to the saturation.
413
414 **4. Discussion**
415 Although, CFWI showed advantages over the coupled inversion of GPR travel time in
416 the presented synthetic study, it is currently still challenging to use CFWI for processing
417 experimental GPR data. Similar to the FWI approach proposed by Klotzsche et al. (2016),
418 the use of CFWI requires an accurate estimation of the source wavelet from the measured
419 GPR data as the GPR waveform does not only depend on the medium properties
420 (dielectric permittivity and electrical conductivity), but also on the source wavelet emitted
421 by the system and the coupling of the antenna and the medium (Busch et al., 2012,
422 Klotzsche et al., 2018). Ineffective source wavelet estimation from measured GPR data
423 will likely result in erroneous simulation of GPR waveform data, and in consequence,
424 will lead to erroneous estimates of the hydraulic parameters using CFWI. In previous
425 studies, the effective source wavelet was estimated using a deconvolution approach,
426 which relies on the measured data and forward modelling based on starting model values.
427 If there are insufficient measurements with varying offsets or angles, it is very difficult to
428 define such starting models, and hence, to obtain effective source wavelets. Therefore,

429 the effective source wavelet is very difficult to estimate from ZOP data. For the GPR data
430 in this study, the phase of the effective source wavelet can be estimated using a starting
431 model where the permittivity is obtained from a ray-based inversion with sufficient
432 accuracy. However, the amplitude of the wavelet is directly coupled to the medium
433 properties and is very sensitive to small changes in the electrical conductivity. To estimate
434 an effective waveform for CFWI, a feasible approach would be to perform MOG
435 measurements. In measurements before measuring the ZOP data or to apply the workflow
436 proposed by Busch et al. (2012) to estimate the source wavelet from the ZOP/ MOG data.
437
438 A second challenge for CFWI is the need for accurate estimation of the electrical
439 conductivity distribution within the soil profile. In this study, the electrical conductivity
440 profiles for GPR modelling were obtained from the corresponding SWC profiles by using
441 Archie's law. However, the uncertainty in Archie's law for estimating soil conductivity
442 from SWC is much greater than that in the petrophysical models relating permittivity and
443 SWC (e.g., CRIM), because the soil electrical conductivity is also sensitive to other
444 factors, e.g., clay content and pore water salinity (Binley et al., 2015). Furthermore,
445 Archie's law does not consider surface electrical conductivity associated with the
446 electrical double layer surrounding soil particles. Advanced petrophysical models should
447 be employed in future studies to consider the influence of the surface conductivity (e.g.,
448 Revil et al., 2007; Mboh et al., 2012). In addition, the electrical conductivity distribution
449 may not only be related to the SWC distribution, because of independent variations in the
450 pore water electrical conductivity associated with fertilizer application or biogeochemical
451 reactions in the subsurface. This potential mismatch between the distribution of electrical
452 conductivity and SWC cannot be neglected in the interpretation of actual infiltration

453 experiments. To accurately describe the electrical conductivity distribution, it may thus
454 be necessary to consider solute transport and geochemical reactions in addition to water
455 flow to predict the distribution of the bulk electrical conductivity in unsaturated soil (e.g.,
456 Loague and Green, 1991). Unfortunately, this will introduce additional unknowns and
457 will undoubtedly increase the difficulty of CFWI. Finally, soils of high salinity or clay
458 content may lead to a strong attenuation of the waveform amplitude. As a result, the noise
459 level of the actual field data measured in these types of soil could be relatively high.
460 Compared to the coupled inversion of the travel times, CFWI may thus be less robust to
461 estimate the hydraulic parameters for these types of soils.
462
463 Finally, it is important to emphasize that CFWI already requires substantial computational
464 resources for the set-up used in this study. CFWI took almost 10 days of computations
465 with a computer cluster (48 processers of AMD Opteron 6300) or a week with the
466 JURECA supercomputer (24 processors) (Jülich Supercomputing Centre, 2018),
467 although the FDTD algorithm in gprMax3D was able to calculate in parallel. Note that
468 further studies should check how this performance can be improved using further
469 parallelization and HPC clusters, for example, the simultaneous parallelization of the
470 SCE-UA and FDTD algorithm. Furthermore, in this study, the grid size was set to 0.02
471 m, which may not be sufficient for accurate GPR simulations in actual 2D or 3D
472 applications of CFWI due to the systematic errors of FDTD algorism caused by the finite-
473 difference discretization and numerical dispersion. If modelling errors need to be further
474 reduced, the discretization of the simulation needs to be refined, which will further
475 increase computational costs. Therefore, it is important to improve the efficiency and
476 accuracy of current GPR modelling methods.

5. Conclusions

In this study, we conducted a synthetic study to explore the feasibility of using CFWI to estimate hydraulic parameters and layer thickness for a 2-layer soil profile. First, a workflow for CFWI was introduced. Compared with the coupled inversion of travel times, CFWI directly uses the entire GPR waveform and can therefore avoid propagation of uncertainties from the picking of first arrivals into the inversion. In a next step, we proposed an infiltration experiment to obtain synthetic vertical SWC profiles based on a real infiltration experiment. This experiment included a 6-hour infiltration event with GPR measurements at three depths (0.2, 0.4, and 0.6 m depth). Based on this experimental design, response surfaces for the layer thickness and different hydraulic parameters were calculated for point SWC measurements, GPR travel times, and GPR waveforms to investigate potential parameter correlations. It was found that layer depth h_t was negatively correlated with θ_{s1} and θ_{s2}. In addition, the response surfaces indicated that CFWI provided more accurate estimates of layer depth compared with coupled inversion of GPR travel times and inversion of point SWC measurements. This is attributed to the fact that CFWI contains additional information introduced by the reflected wave from the layer boundary. Finally, CFWI and coupled inversion of GPR travel times were applied to the synthetic infiltration experiment. The simulated waveforms and travel times matched well with the noisy data, but the estimates of the hydraulic parameters from the coupled inversion of travel times showed a slight deviation from the true values and a relatively larger uncertainty in the hydraulic conductivity and retention functions. On the other hand, hydraulic parameters estimated from CFWI had considerably smaller uncertainty and thus better matched the known water retention and hydraulic conductivity

curves. However, a range of challenges remain for the application of CFWI to real field experiments. First, a robust approach for effective source wavelet estimation for measured ZOP data has to be developed. Moreover, the use of a more sophisticated hydrological model that couples the simulations of water flow and solute transport has to be considered for CFWI to cope with changes in electrical conductivity associated with fertilization and geochemical processes. In addition, the efficiency of the current GPR modelling has to be improved. In conclusion, CFWI has several advantages over the coupled inversion of GPR travel times and it is expected to be a promising inversion approach for estimating hydraulic parameters at field scale after several remaining challenges have been addressed.

Acknowledgement

The first author is supported by a CSC scholarship (grant number: No. 201606410058). This study was also funded by the Deutsche Forschungsgemeinschaft (DFG, German Research Foundation) under Germany's Excellence Strategy - EXC 2070 – 390732324. The authors acknowledge the computing time granted by the John von Neumann Institute for Computing (NIC) and provided on the supercomputer JURECA of the Jülich Supercomputing Centre (JSC).

Reference

Archie, G.E., 1942. The electrical resistivity log as an aid in determining some reservoir characteristics. Transactions of the AIME. 146(01): 54-62.

Bano, M., 2006. Effects of the transition zone above a water table on the reflection of GPR waves. Geophysical Research Letters. 33(13). doi:10.1029/2006GL026158

527 Berkhout, A.J., 2012. Combining full wavefield migration and full waveform inversion,
528 a glance into the future of seismic imaging. Geophysics. 77(2): S43-S50.
529 doi:10.1190/geo2011-0148.1
530
531 Binley, A., Hubbard, S.S., Huisman, J.A., Revil, A., Robinson, D.A., Singha, K., Slater,
532 L.D., 2015. The emergence of hydrogeophysics for improved understanding of
533 subsurface processes over multiple scales. Water Resour. Res. 51(6): 3837-3866.
534 doi:10.1002/2015WR017016
535
536 Binley, A., Winship, P., Middleton, R., Pokar, M., West, J., 2001. High-resolution
537 characterization of vadose zone dynamics using cross-borehole radar. Water Resour. Res.
538 37(11): 2639-2652. doi:10.1029/2000WR000089
539
540 Bradford, J.H., 2008. Measuring Water Content Heterogeneity Using Multifold GPR with
541 Reflection Tomography. Vadose Zone J. 7(1): 184-193. doi:10.2136/vzj2006.0160
542
543 Brossier, R., Operto, S., Virieux, J., 2009. Seismic imaging of complex onshore structures
544 by 2D elastic frequency-domain full-waveform inversion. Geophysics. 74(6): WCC105-
545 WCC118. doi:10.1190/1.3215771
546
547 Busch, S., van der Kruk, J., Vereecken, H., 2014. Improved characterization of fine-
548 texture soils using on-ground GPR full-waveform inversion. IEEE Trans. Geosci. Remote
549 Sens. 52(7): 3947-3958. doi:10.1109/TGRS.2013.2278297
550
551 Busch, S., van der Kruk, J., Bikowski, J., Vereecken, H., 2012. Quantitative conductivity
552 and permittivity estimation using full-waveform inversion of on-ground GPR data.
553 Geophysics. 77(6): H79-H91. doi:10.1190/geo2012-0045.1
554
555 Busch, S., Weihermüller, L., Huisman, J.A., Steelman, C.M., Endres, A.L., Vereecken,
556 H., van der Kruk, J., 2013. Coupled hydrogeophysical inversion of time-lapse surface
557 GPR data to estimate hydraulic properties of a layered subsurface. Water Resour. Res.
558 49(12): 8480-8494. doi:10.1002/2013wr013992

559
560 Cai, G., Vanderborght, J., Couvreur, V., Mboh, C.M., Vereecken, H., 2018.
561 Parameterization of root water uptake models considering dynamic root distributions and
562 water uptake compensation. Vadose Zone J. 17(1): 160125. doi:10.2136/vzj2016.12.0125
563
564 Jülich Supercomputing Centre, 2018. Jureca: Modular supercomputer at jülich
565 supercomputing centre. J. Large-Scale Res. Fac. 4: 132. doi:10.17815/jlsrf-4-121-1
566
567 Daniels, D.J., 2005, Ground penetrating radar, Encyclopedia of RF and Microwave
568 Engineering. doi:10.1002/0471654507.eme152
569
570 Diouf, O.C., Weihermüller, L., Diedhiou, M., Vereecken, H., Faye, S.C., Faye, S., Sylla,
571 S.N., 2020. Modelling groundwater evapotranspiration in a shallow aquifer in a semi-arid
572 environment. J. Hydrol. 587: 124967. doi:10.1016/j.jhydrol.2020.124967
573
574 Duan, Q.Y., Gupta, V.K., Sorooshian, S., 1993. Shuffled complex evolution approach for
575 effective and efficient global minimization. J. Optimiz. Theory. App. 76(3): 501-521.
576 doi:10.1007/BF00939380
577
578 Doble, R.C., Crosbie, R.S., 2017. Review: Current and emerging methods for catchment-
579 scale modelling of recharge and evapotranspiration from shallow groundwater.
580 Hydrogeol. J. 25(1): 3-23. doi:10.1007/s10040-016-1470-3
581
582 Doolittle, J.A., Jenkinson, B., Hopkins, D., Ulmer, M., Tuttle, W., 2006.
583 Hydropedological investigations with ground-penetrating radar (GPR): Estimating water-
584 table depths and local ground-water flow pattern in areas of coarse-textured soils.
585 Geoderma. 131(3): 317-329. doi:10.1016/j.geoderma.2005.03.027
586
587 Ernst, J.R., Green, A.G., Maurer, H., Holliger, K., 2007a. Application of a new 2D time-
588 domain full-waveform inversion scheme to crosshole radar data. Geophysics. 72(5): J53-
589 J64. doi:10.1190/1.2761848
590

591 Ernst, J.R., Maurer, H., Green, A.G., Holliger, K., 2007b. Full-waveform inversion of
592 crosshole radar data based on 2-D finite-difference time-domain solutions of Maxwell's
593 equations. IEEE Trans. Geosci. Remote Sens. 45(9): 2807-2828.
594 doi:10.1109/TGRS.2007.901048
595
596 Ewing, R.P., Hunt, A.G., 2006. Dependence of the electrical conductivity on saturation
597 in real porous media. Vadose Zone J. 5(2): 731-741. doi:10.2136/vzj2005.0107
598
599 Galagedara, L., Parkin, G., Redman, J., Endres, A., 2002. Temporal and spatial variation
600 of soil water content measured by borehole GPR under irrigation and drainage, Ninth
601 International Conference on Ground Penetrating Radar (GPR2002). SPIE, pp. 180–185.
602 doi:10.1117/12.462253.
603
604 Giannopoulos, A., 2005. Modelling ground penetrating radar by GprMax. Constr. Build
605 Mater. 19(10): 755-762. doi:10.1016/j.conbuildmat.2005.06.007
606
607 Gómez-Hernández, J.J., Gorelick, S.M., 1989. Effective groundwater model parameter
608 values: Influence of spatial variability of hydraulic conductivity, leakance, and recharge.
609 Water Resour. Res. 25(3): 405-419. doi:10.1029/WR025i003p00405
610
611 Gueting, N., Vienken, T., Klotzsche, A., van der Kruk, J., Vanderborght, J., Caers, J.,
612 Vereecken, H., Englert, A., 2017. High resolution aquifer characterization using
613 crosshole GPR full-waveform tomography: Comparison with direct-push and tracer test
614 data. Water Resour. Res. 53(1): 49-72. doi:10.1002/2016WR019498
615
616 Hinnell, A.C., Ferré, T.P.A., Vrugt, J.A., Huisman, J.A., Moysey, S., Rings, J., Kowalsky,
617 M.B., 2010. Improved extraction of hydrologic information from geophysical data
618 through coupled hydrogeophysical inversion. Water Resour. Res. 46(4).
619 doi:10.1029/2008wr007060
620
621 Huisman, J.A., Hubbard, S.S., Redman, J.D., Annan, A.P., 2003. Measuring soil water
622 content with ground penetrating radar: A Review. Vadose Zone J. 2(4): 476-491.

623 doi:10.2136/vzj2003.4760
624
625 Huisman, J.A., Rings, J., Vrugt, J.A., Sorg, J., Vereecken, H., 2010. Hydraulic properties
626 of a model dike from coupled Bayesian and multi-criteria hydrogeophysical inversion. J.
627 Hydrol. 380(1): 62-73. doi:10.1016/j.jhydrol.2009.10.023
628
629 Ihamouten, A., Bosc, F., Guan, B., Le Bastard, C., Fauchard, C., Lambot, S., Dérobert,
630 X., 2018. Full-waveform inversion using a stepped-frequency GPR to characterize the
631 tack coat in hot-mix asphalt (HMA) layers of flexible pavements. NDT E Int. 95: 17-25.
632 doi:10.1016/j.ndteint.2017.12.006
633
634 Irving, J.D., Knoll, M.D., Knight, R.J., 2007. Improving crosshole radar velocity
635 tomograms: A new approach to incorporating high-angle traveltime data. Geophysics.
636 72(4): J31-J41. doi:10.1190/1.2742813
637
638 Jadoon, K.Z., Slob, E., Vanclooster, M., Vereecken, H., Lambot, S., 2008. Uniqueness
639 and stability analysis of hydrogeophysical inversion for time-lapse ground-penetrating
640 radar estimates of shallow soil hydraulic properties. Water Resour. Res. 44(9).
641 doi:10.1029/2007WR006639
642
643 Jadoon, K.Z., Weihermüller, L., Scharnagl, B., Kowalsky, M.B., Bechtold, M., Hubbard,
644 S.S., Vereecken, H., Lambot, S., 2012. Estimation of soil hydraulic parameters in the field
645 by integrated hydrogeophysical inversion of time-lapse ground-penetrating radar data.
646 Vadose Zone J. 11(4): vzj2011.0177. doi:10.2136/vzj2011.0177
647
648 Klotzsche, A., Jonard, F., Looms, M.C., van der Kruk, J., Huisman, J.A., 2018. Measuring
649 soil water content with ground penetrating radar: A decade of progress. Vadose Zone J.
650 17(1): 180052. doi:10.2136/vzj2018.03.0052
651
652 Klotzsche, A., van der Kruk, J.., He, G., Vereecken, H., 2016. GPR full-waveform
653 inversion of horizontal ZOP borehole data using GprMax, 2016 16th International
654 Conference on Ground Penetrating Radar (GPR), pp. 1-5.

655 doi:10.1109/ICGPR.2016.7572695
656
657 Klotzsche, A., van der Kruk, J.., Linde, N., Doetsch, J., Vereecken, H., 2013. 3-D
658 characterization of high-permeability zones in a gravel aquifer using 2-D crosshole GPR
659 full-waveform inversion and waveguide detection. Geophysical Journal International.
660 195(2): 932-944. doi:10.1093/gji/ggt275
661
662 Klotzsche, A., van der Kruk, J., Angelo Meles, G., Doetsch, J., Maurer, H., Linde, N.,
663 2010. Full-waveform inversion of cross-hole ground-penetrating radar data to
664 characterize a gravel aquifer close to the Thur River, Switzerland. Near Surf. Geophys.
665 8(6): 635-649. doi:10.3997/1873-0604.2010054
666
667 Klotzsche, A., van der Kruk, J., Bradford, J., Vereecken, H., 2014. Detection of spatially
668 limited high-porosity layers using crosshole GPR signal analysis and full-waveform
669 inversion. Water Resour. Res. 50(8): 6966-6985. doi:10.1002/2013WR015177
670
671 Klotzsche, A., Vereecken, H., van der Kruk, J., 2019a. Review of crosshole ground-
672 penetrating radar full-waveform inversion of experimental data: Recent developments,
673 challenges, and pitfalls. Geophysic. 84(6): H13-H28. doi:10.1190/geo2018-0597.1
674
675 Klotzsche, A., Lärm, L., Vanderborght, J., Cai, G., Morandage, S., Zörner, M., Vereecken,
676 H., van der Kruk, J., 2019b. Monitoring soil water content using time-lapse horizontal
677 borehole GPR data at the field-plot scale. Vadose Zone J. 18(1): 190044.
678 doi:10.2136/vzj2019.05.0044
679
680 Kool, J.B., Parker, J.C., 1988. Analysis of the inverse problem for transient unsaturated
681 flow. Water Resour. Res. 24(6): 817-830. doi:10.1029/WR024i006p00817
682
683 Kowalsky, M.B., Finsterle, S., Peterson, J., Hubbard, S., Rubin, Y., Majer, E., Ward, A.,
684 Gee, G., 2005. Estimation of field-scale soil hydraulic and dielectric parameters through
685 joint inversion of GPR and hydrological data. Water Resour. Res. 41(11).
686 doi:10.1029/2005wr004237

Kowalsky, M.B., Finsterle, S., Rubin, Y., 2004. Estimating flow parameter distributions using ground-penetrating radar and hydrological measurements during transient flow in the vadose zone. Adv. Water Resour. 27(6): 583-599. doi:10.1016/j.advwatres.2004.03.003

Lambot, S., André, F., 2014. Full-wave modeling of near-field radar data for planar layered media reconstruction. IEEE Trans. Geosci. Remote Sens. 52(5): 2295-2303. doi:10.1109/TGRS.2013.2259243

Lambot, S., Slob, E., Rhebergen, J., Lopera, O., Jadoon, K.Z., Vereecken, H., 2009. Remote estimation of the hydraulic properties of a sand using full-waveform integrated hydrogeophysical inversion of time-Lapse, off-Ground GPR data. Vadose Zone J. 8(3): 743-754. doi:10.2136/vzj2008.0058

Lambot, S., Slob, E.C., Vanclooster, M., Vereecken, H., 2006. Closed loop GPR data inversion for soil hydraulic and electric property determination. Geophys. Res. Lett. 33(21). doi:10.1029/2006GL027906

Li, D., Xu, K., Harris, J.M., Darve, E., 2020. Coupled time-lapse full-waveform inversion for subsurface flow problems using intrusive automatic differentiation. Water Resour. Res. 56(8): e2019WR027032. doi:10.1029/2019wr027032

Liu, T., Klotzsche, A., Pondkule, M., Vereecken, H., Su, Y., van der Kruk, J., 2018. Radius estimation of subsurface cylindrical objects from ground-penetrating-radar data using full-waveform inversion. Geophysics. 83(6): H43-H54. doi:10.1190/geo2017-0815.1

Loague, K., Green, R.E., 1991. Statistical and graphical methods for evaluating solute transport models: Overview and application. J. Contam. Hydrol. 7(1): 51-73. doi:10.1016/0169-7722(91)90038-3

719 Looms, M.C., Binley, A., Jensen, K.H., Nielsen, L., Hansen, T.M., 2008. Identifying
720 unsaturated hydraulic parameters using an integrated data fusion approach on cross-
721 borehole geophysical data. Vadose Zone J. 7(1): 238-248. doi:10.2136/vzj2007.0087
722
723 Looms, M.C., Klotzsche, A., van der Kruk, J., Larsen, T.H., Edsen, A., Tuxen, N.,
724 Hamburger, N., Keskinen, J., Nielsen, L., 2017. Mapping sand layers in clayey till using
725 crosshole ground-penetrating radar. Geophysics. 83(1): A21-A26. doi:10.1190/geo2017-
726 0297.1
727
728 Mboh, C.M., Huisman, J.A., Van Gaelen, N., Rings, J., Vereecken, H., 2012. Coupled
729 hydrogeophysical inversion of electrical resistances and inflow measurements for topsoil
730 hydraulic properties under constant head infiltration. Near Surf. Geophys. 10(5): 413-426.
731 doi:10.3997/1873-0604.2012009
732
733 Meles, G.A., van der Kruk, J.., Greenhalgh, S.A., Ernst, J.R., Maurer, H., Green, A.G.,
734 2010. A new vector waveform inversion algorithm for simultaneous updating of
735 conductivity and permittivity parameters from combination crosshole/borehole-to-
736 surface GPR data. IEEE Trans. Geosci. Remote Sens. 48(9): 3391-3407.
737 doi:10.1109/TGRS.2010.2046670
738
739 Mualem, Y., 1976. A new model for predicting the hydraulic conductivity of unsaturated
740 porous media. Water Resour. Res. 12(3): 513-522. doi:10.1029/WR012i003p00513
741
742 Peleg, N., Gvirtzman, H., 2010. Groundwater flow modeling of two-levels perched
743 karstic leaking aquifers as a tool for estimating recharge and hydraulic parameters. J.
744 Hydrol. 388(1): 13-27. doi:10.1016/j.jhydrol.2010.04.015
745
746 Pollacco, J.A.P., Ugalde, J.M.S., Angulo-Jaramillo, R., Braud, I., Saugier, B., 2008. A
747 Linking Test to reduce the number of hydraulic parameters necessary to simulate
748 groundwater recharge in unsaturated soils. Adv. Water Resour. 31(2): 355-369. doi:
749 10.1016/j.advwatres.2007.09.002
750

751 Revil, A., Linde, N., Cerepi, A., Jougnot, D., Matthäi, S., Finsterle, S., 2007.
752 Electrokinetic coupling in unsaturated porous media. J. Colloid Interface Sci. 313(1):
753 315-327. doi:10.1016/j.jcis.2007.03.037
754
755 Rossi, M., Manoli, G., Pasetto, D., Deiana, R., Ferraris, S., Strobbia, C., Putti, M.,
756 Cassiani, G., 2015. Coupled inverse modeling of a controlled irrigation experiment using
757 multiple hydro-geophysical data. Adv. Water Resour. 82: 150-165.
758 doi:10.1016/j.advwatres.2015.03.008
759
760 Roth, K., Schulin, R., Flühler, H., Attinger, W., 1990. Calibration of time domain
761 reflectometry for water content measurement using a composite dielectric approach.
762 Water Resour. Res. 26(10): 2267-2273. doi:10.1029/WR026i010p02267
763
764 Rucker, D.F., Ferré, T.P.A., 2004. Parameter estimation for soil hydraulic properties
765 using zero-offset borehole radar. Soil Sci. Soc. Am. J. 68(5): 1560-1567.
766 doi:10.2136/sssaj2004.1560
767
768 Scholer, M., Irving, J., Looms, M.C., Nielsen, L., Holliger, K., 2013. Examining the
769 information content of time-lapse crosshole GPR data collected under different
770 infiltration conditions to estimate unsaturated soil hydraulic properties. Adv. Water
771 Resour. 54: 38-56. doi:10.1016/j.advwatres.2012.12.011
772
773 Shinomiya, Y., Takahashi, K., Kobiyama, M., Kubota, J., 2001. Evaluation of the
774 tortuosity parameter for forest soils to predict unsaturated hydraulic conductivity. J. For.
775 Res. 6(3): 221-225. doi:10.1007/BF02767097
776
777 Šimůnek, J., van Genuchten, M.T., Šejna, M., 2008. Development and applications of the
778 HYDRUS and STANMOD software packages and related codes. Vadose Zone J. 7(2):
779 587-600. doi:10.2136/vzj2007.0077
780
781 Tarantola, A., 1984. Inversion of seismic reflection data in the acoustic approximation.
782 Geophysics. 49(8): 1259-1266. doi:10.1190/1.1441754

783
784 Topp, G.C., Davis, J.L., Annan, A.P., 1980. Electromagnetic determination of soil water
785 content: Measurements in coaxial transmission lines. Water Resour. Res. 16(3): 574-582.
786 doi:10.1029/WR016i003p00574
787
788 Topp, G.C., Ferré, T.P.A., 2005. Time-domain reflectometry. Encyclopedia of Soils in
789 the Environment. Elsevier, Oxford, pp. 174-181. doi:10.1016/B0-12-348530-4/00508-7
790
791 van Genuchten, M.T., 1980. A closed-form equation for predicting the hydraulic
792 conductivity of unsaturated soils. Soil Sci. Soc. Am. J. 44(5): 892-898.
793 doi:10.2136/sssaj1980.03615995004400050002x
794
795 Vigh, D., Starr, E.W., 2008. 3D prestack plane-wave, full-waveform inversion.
796 Geophysics. 73(5): VE135-VE144. doi:10.1190/1.2952623
797
798 Virieux, J., Operto, S., 2009. An overview of full-waveform inversion in exploration
799 geophysics. Geophysics. 74(6): WCC1-WCC26. doi:10.1190/1.3238367
800
801 Vrugt, J., Dane, J., 2006. Inverse modeling of soil hydraulic properties, In Encyclopedia
802 of Hydrological Sciences. doi:10.1002/0470848944.hsa079
803
804 Warnick, K.F., 2005. An intuitive error analysis for FDTD and comparison to MoM.
805 IEEE Antennas Propag. Mag. 47(6): 111-115. doi:10.1109/MAP.2005.1608751
806
807 Warren, C., Giannopoulos, A., Giannakis, I., 2016. gprMax: Open source software to
808 simulate electromagnetic wave propagation for Ground Penetrating Radar. Comput. Phys.
809 Commun. 209: 163-170. doi:10.1016/j.cpc.2016.08.020
810
811 Yu, Y., Klotzsche, A., Weihermüller, L., Huisman, J.A., Vanderborght, J., Vereecken, H.,
812 van der Kruk, J., 2020. Measuring vertical soil water content profiles by combining
813 horizontal borehole and dispersive surface ground penetrating radar data. Near Surf.
814 Geophys. 18(3): 275-294. doi:10.1002/nsg.12099

Yu, Y., Weihermüller, L., Klotzsche, A., Lärm, L., Vereecken, H., Huisman, J.A., 2021. Sequential and coupled inversion of horizontal borehole ground penetrating radar data to estimate soil hydraulic properties at the field scale. J. Hydrol. 596: 126010. doi:10.1016/j.jhydrol.2021.126010

Figure

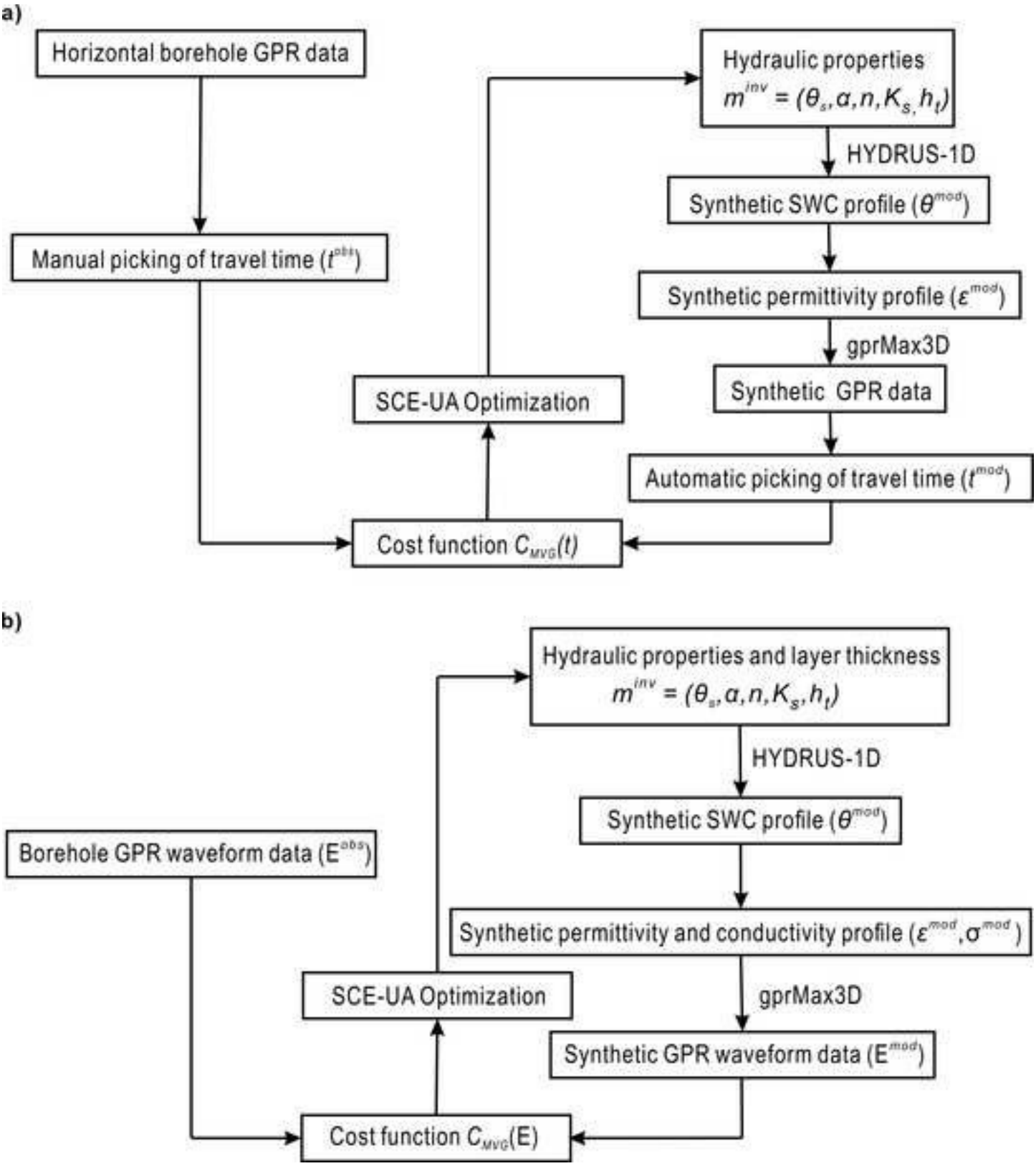

Figure

Click here to access/download;Figure;Fig_2.tif

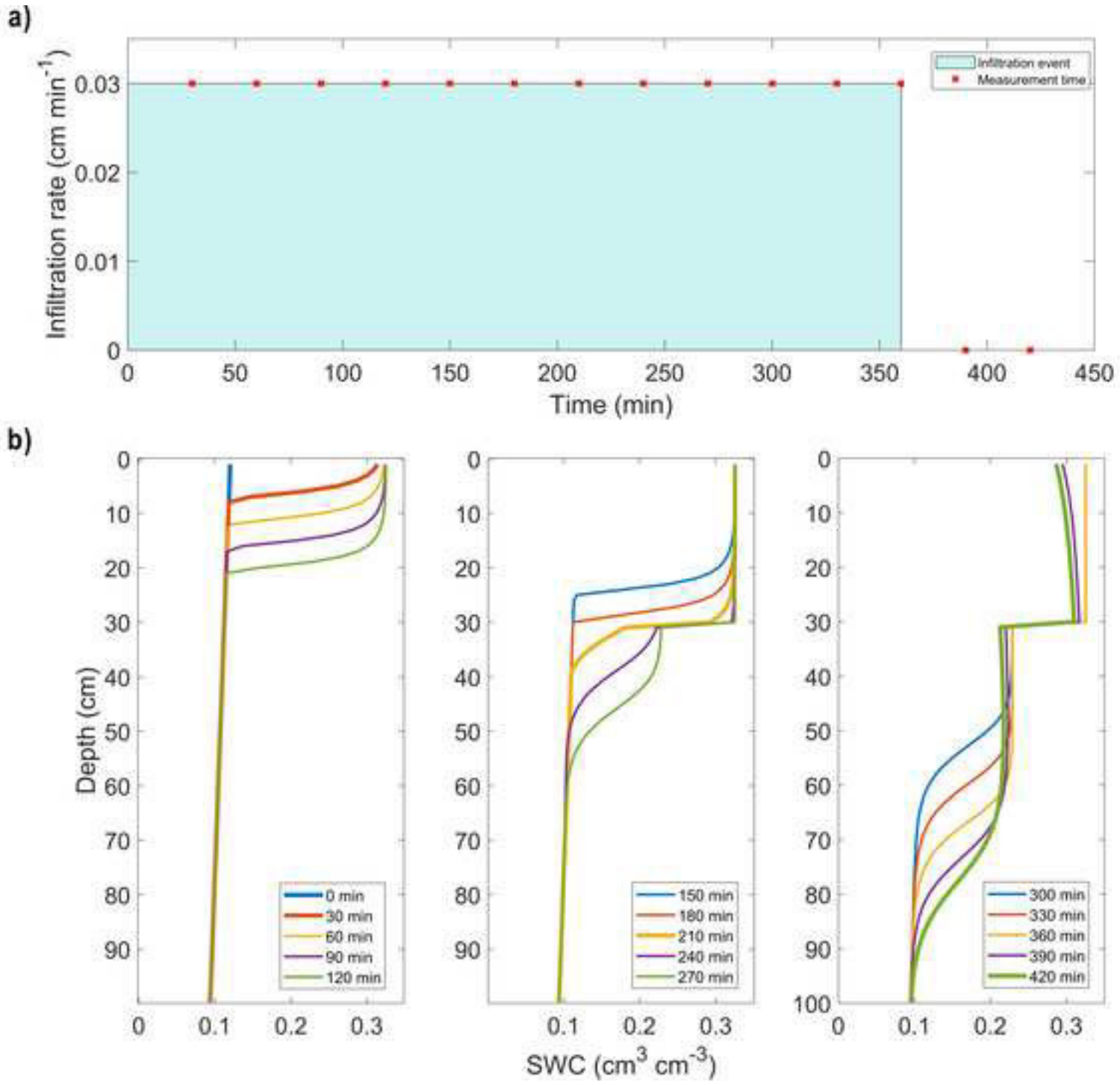

Figure

Click here to access/download;Figure;Fig_3.tif

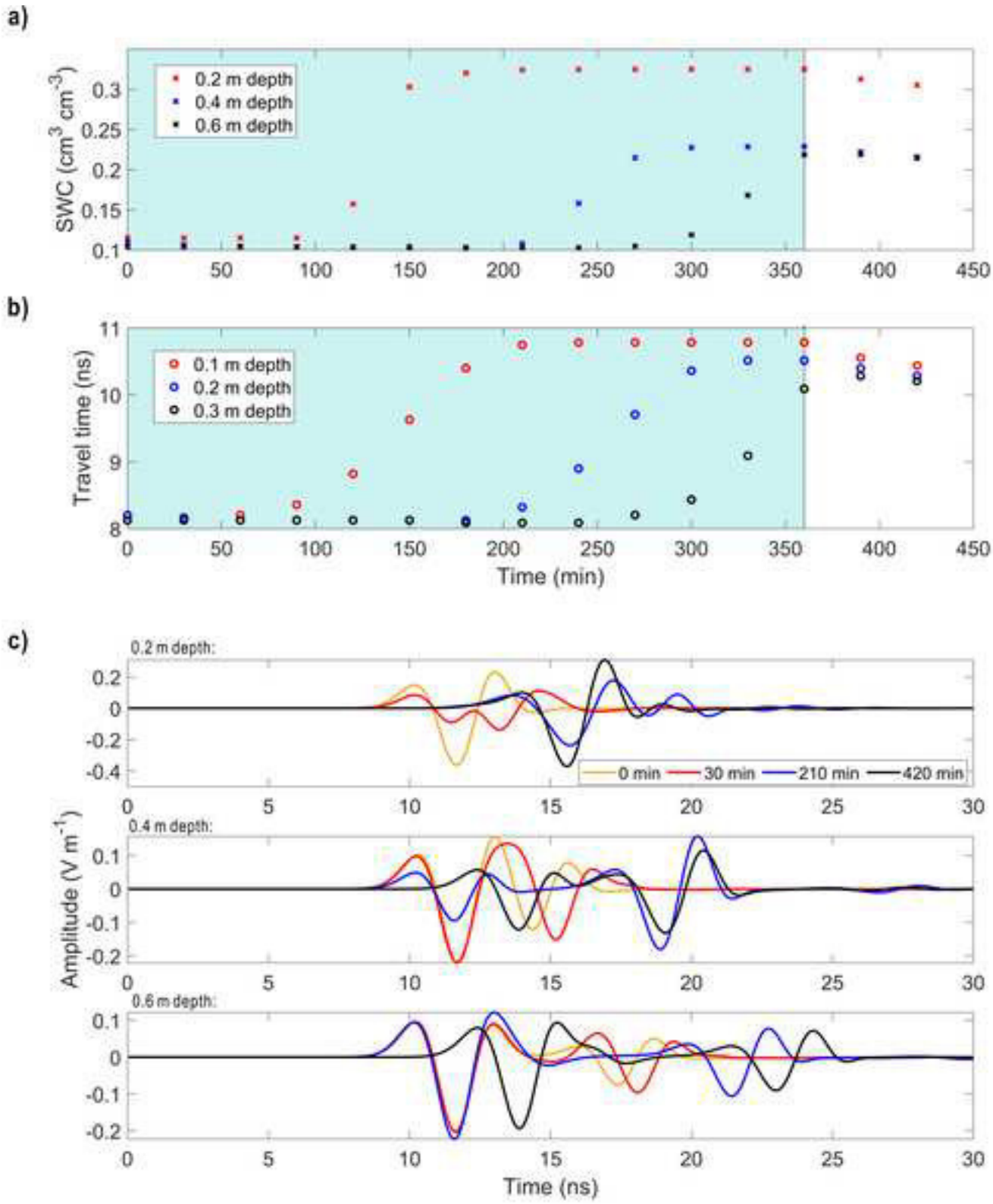

Figure

Click here to access/download;Figure;Fig_4.tif

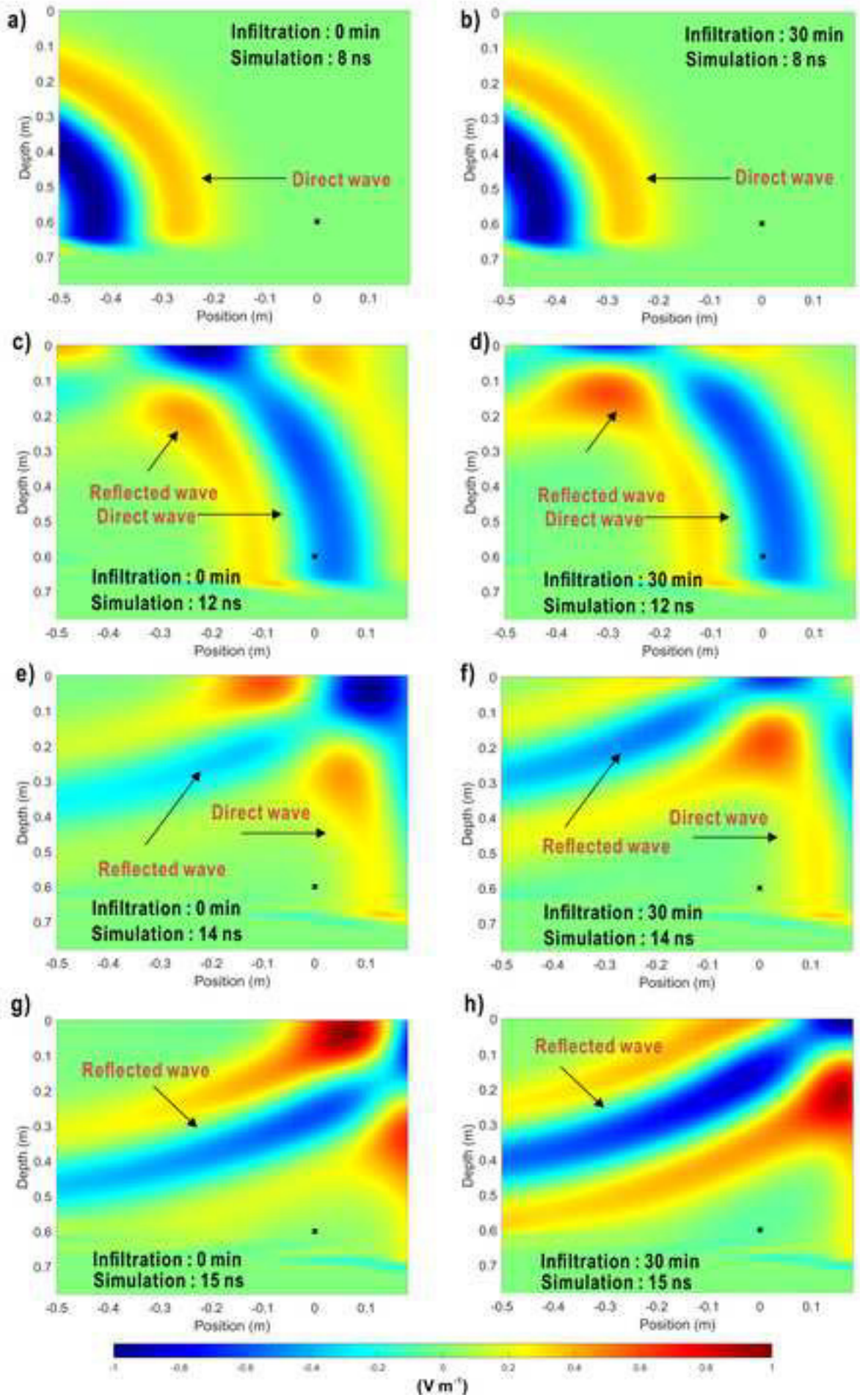

Figure

Click here to access/download;Figure;Fig_5.tif

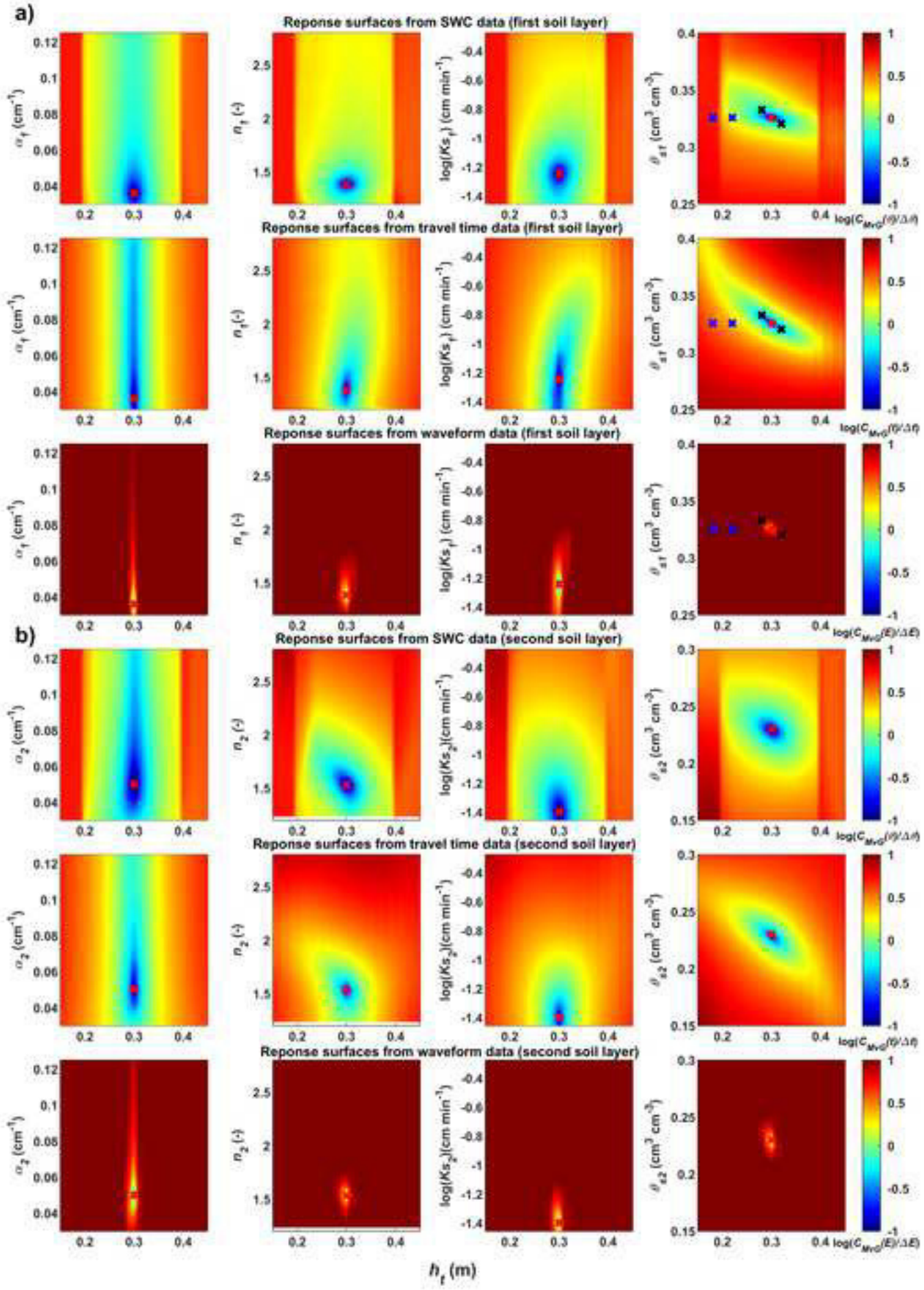

Figure

Click here to access/download;Figure;Fig_6.tif

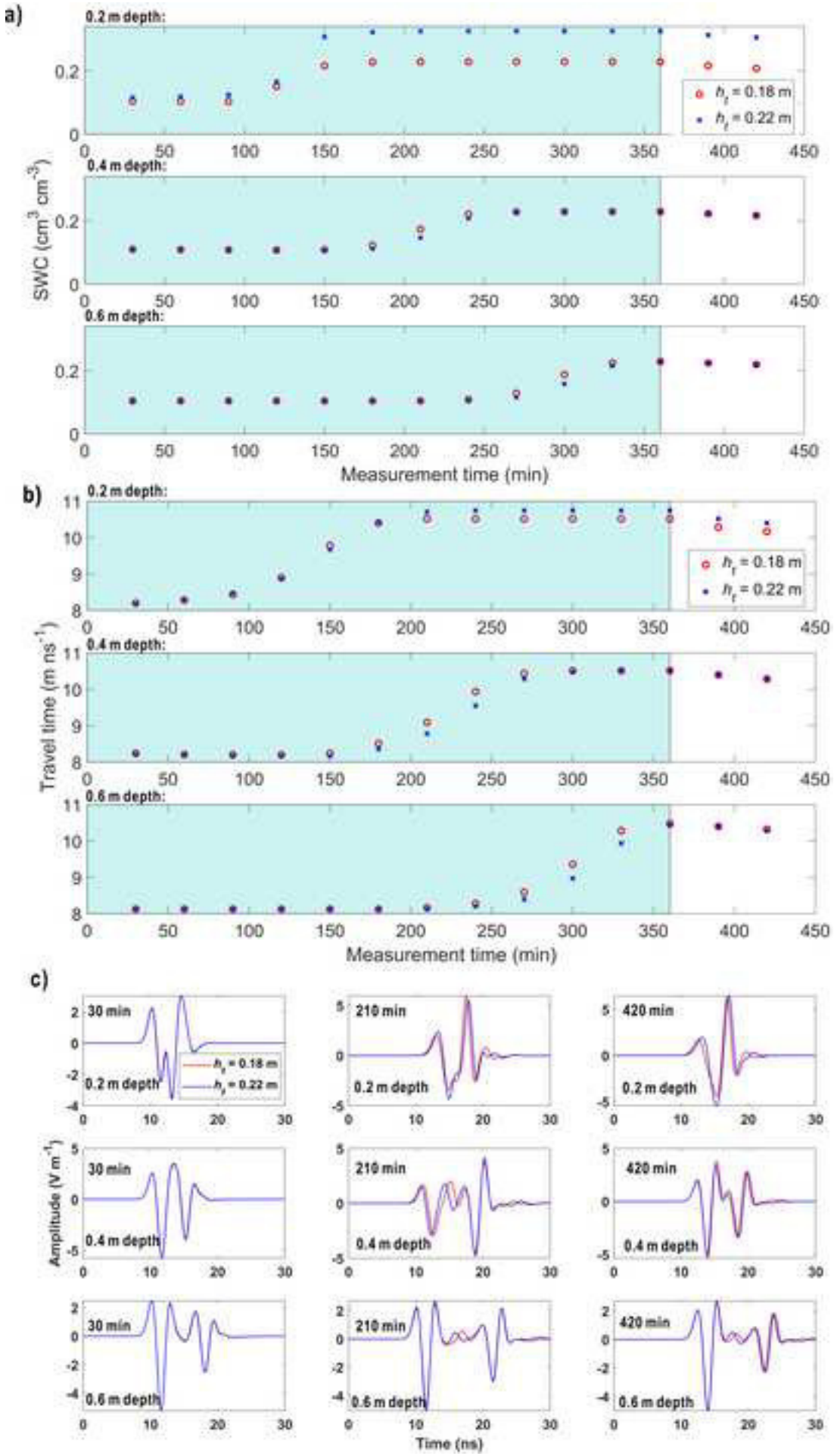

Figure

Click here to access/download;Figure;Fig_7.tif

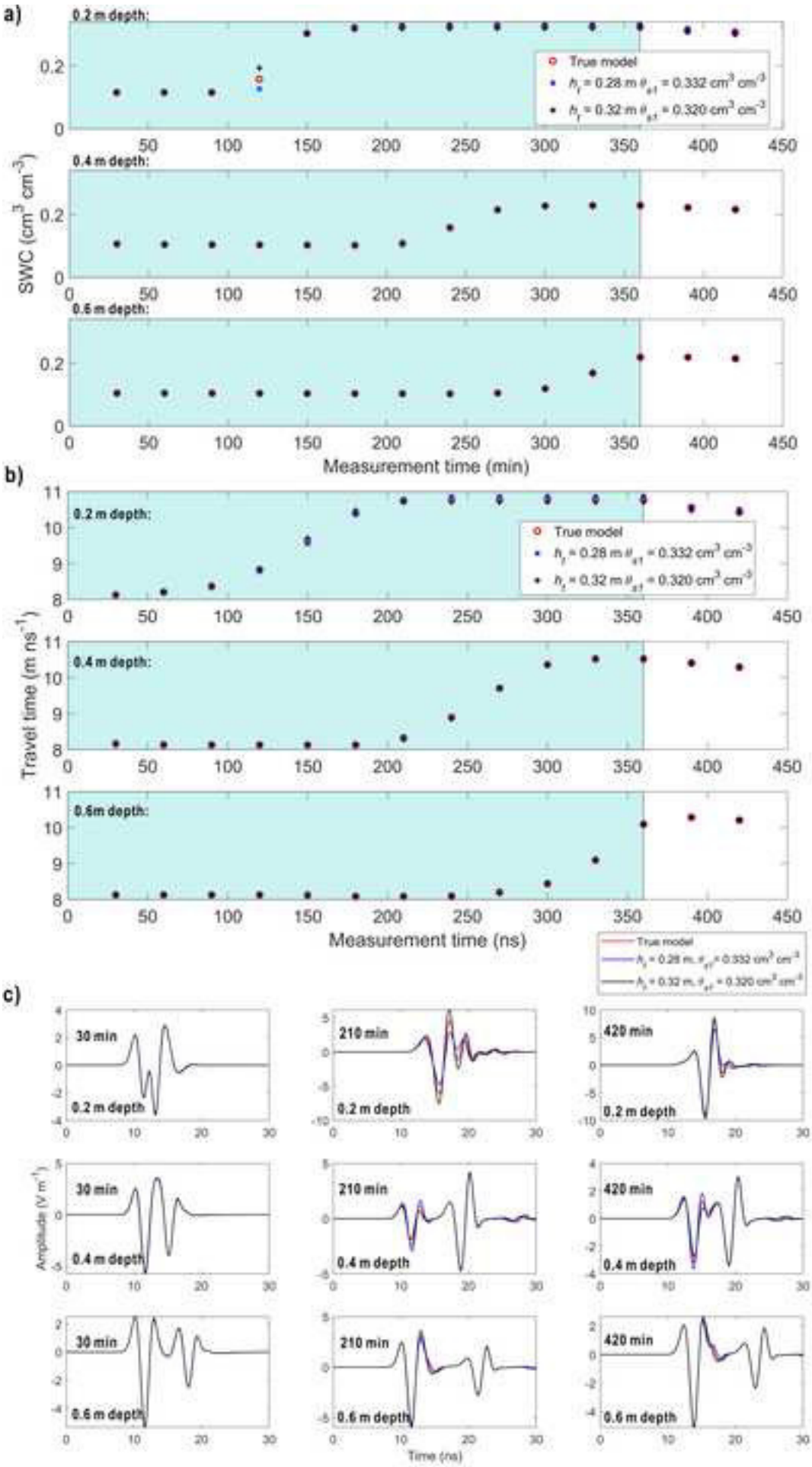

Figure

Click here to access/download;Figure;Fig_8.tif

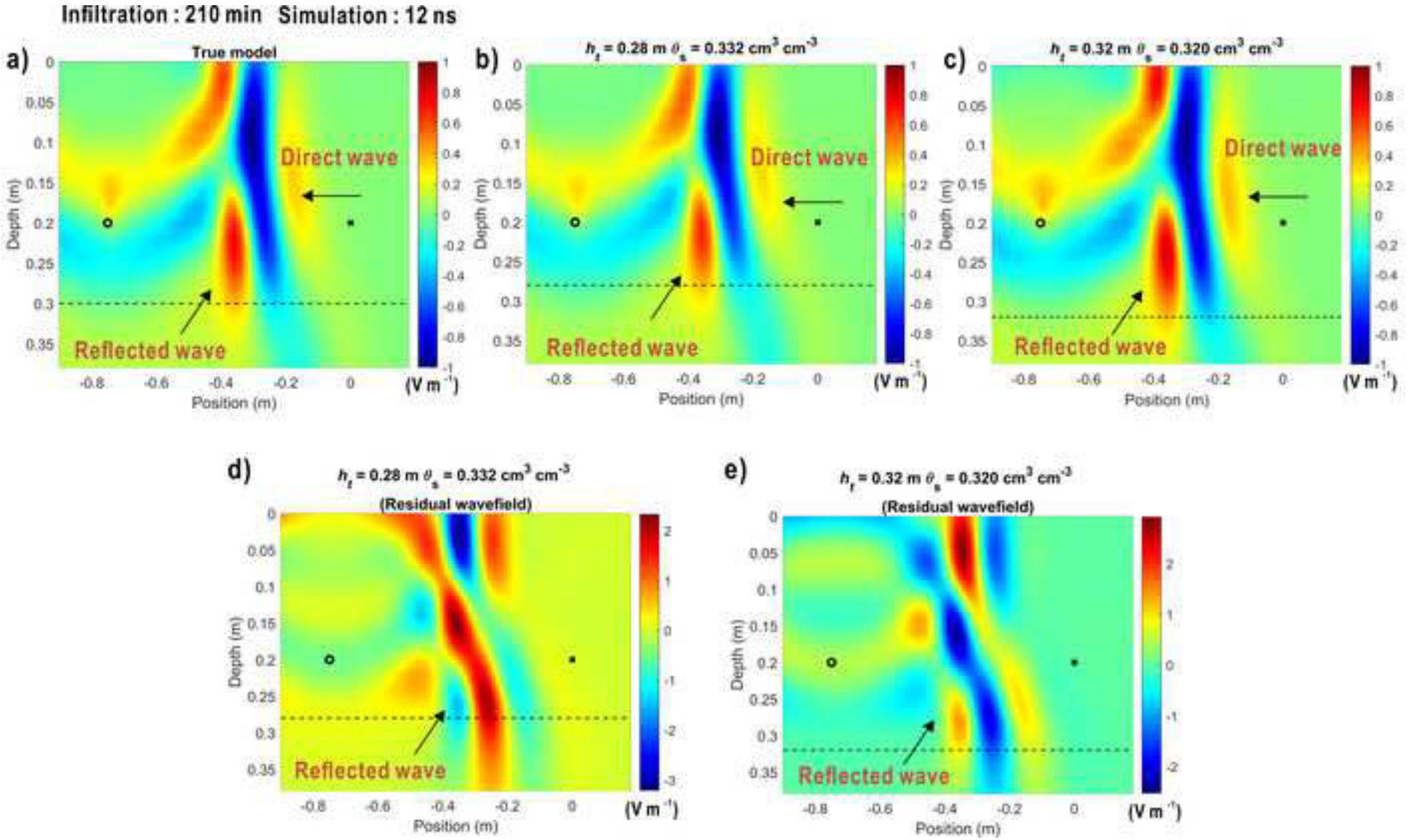

Figure

Click here to access/download;Figure;Fig_9.tif

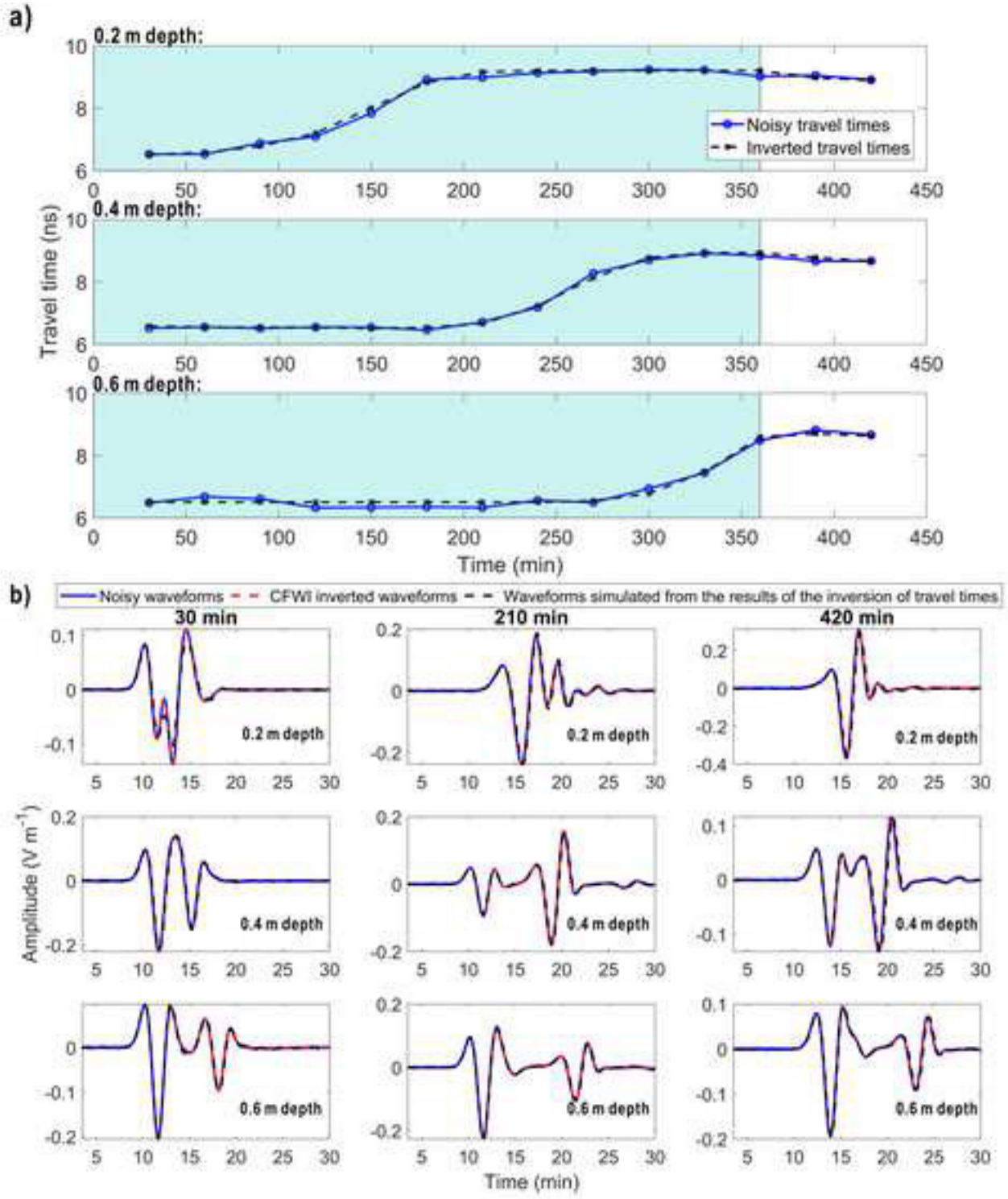

Figure

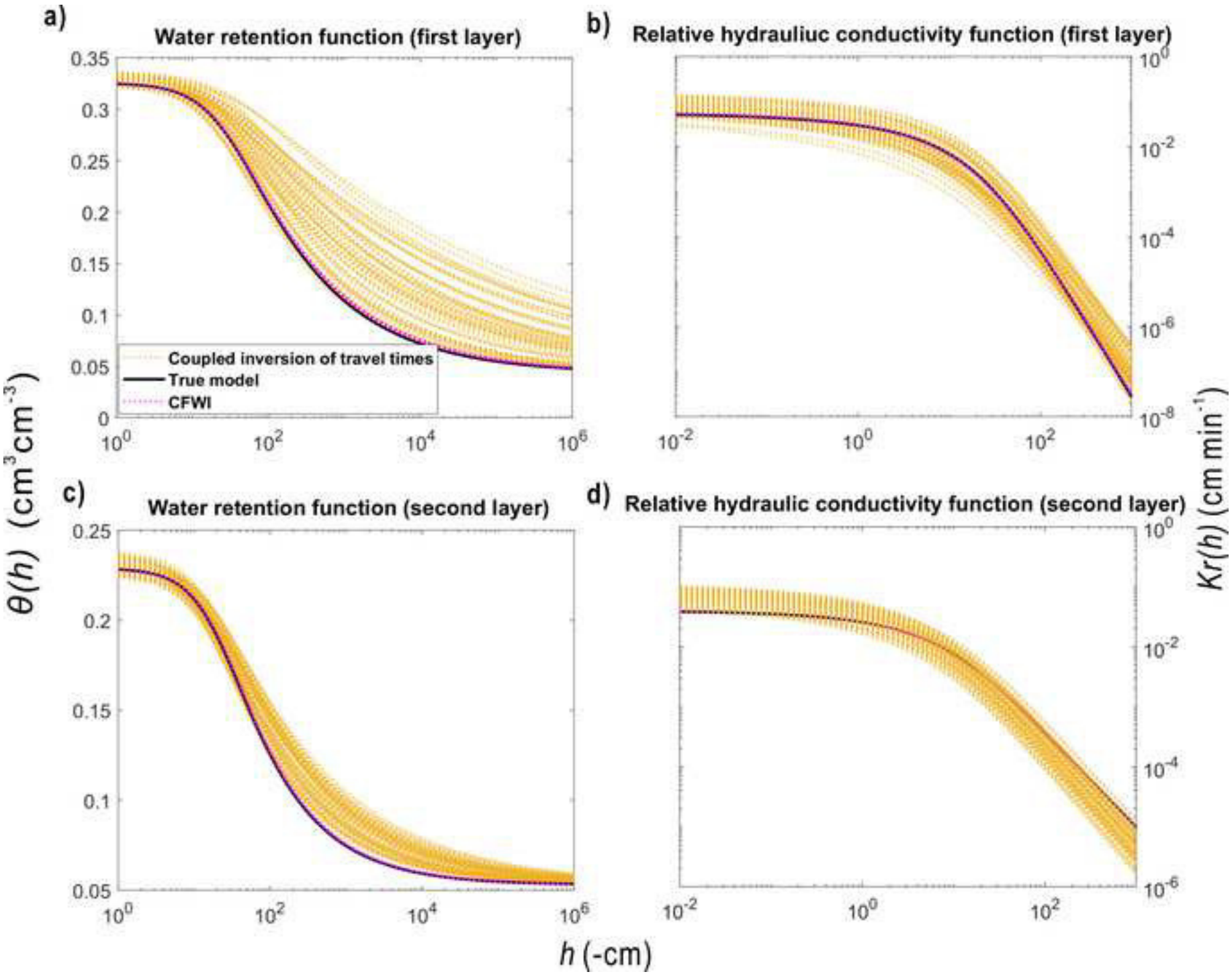

Fig. 1 Flowchart of (a) coupled inversion of GPR travel times (adapted from Yu et al. (2021)) and (b) coupled full waveform inversion (CFWI).

Fig. 2 (a) Schedule of the infiltration experiment and synthetic GPR measurements. (b) Synthetic vertical SWC profiles obtained with HYDRUS-1D at the time of the GPR measurements obtained with the hydraulic parameters provided in Table. 1. The vertical SWC profiles (0 min, 30 min, 210 min and 420 min) used to generate GPR waveforms were shown with a larger linewidth.

Fig. 3 (a) Synthetic time-lapse SWC data at 0.2, 0.4, and 0.6 m depths. The timing of the infiltration event is indicated by the light green background. (b) GPR travel times obtained from synthetic GPR data based on vertical water content distributions used as inputs in gprMax3D. (c) Synthetic GPR waveform data obtained at four different measurement times.

Fig. 4 Snapshots of the GPR wavefields for a transmitter and receiver position at 0.6 m depth. Wavefields are shown for (a, b) 8 ns, (c, d) 12 ns, (e, f) 14 ns and (g, h) 15 ns for two different measurement times (0 and 30 min) of the infiltration experiment. Note, the fields simulated at the same propagation time (e.g., a, b) were normalized by the maximum field value for the 0 min of that propagation time (e.g., a) to allow a better comparison of the amplitude changes for different measurement times. The position of the receiver antenna is indicated by the black cross. Note that the transmitter is located at a position of -0.75 m at a depth of 0.6 m.

Fig. 5 Response surfaces for layer thickness (h_t) and different hydraulic parameters of the (a) first layer and (b) second layer for GPR waveforms, GPR travel times, and SWC. The cost function values were normalized by their noise level and were shown in logarithmic scale. Using this normalization, the areas enclosed by green can qualitatively be interpreted as the parameter uncertainty. The true model is shown by the red cross. In the response surfaces for $h_t - \theta_{s1}$ the black crosses refer to the models of 0.28 m (0.332 cm^3cm^{-3}) and 0.32 m (0.320 cm^3cm^{-3}) and the blue crosses refer to the models of 0.18 m (0.326 cm^3cm^{-3}) and 0.22 m (0.326 cm^3cm^{-3}).

Fig. 6 (a) SWC data, (b) synthetic travel times, and (c) synthetic GPR waveforms at three different times calculated according to the models indicated by the blue crosses in Fig. 5. The length of the infiltration event is indicated by the light green background.

Fig. 7 (a) SWC data, (b) synthetic travel times and (c) synthetic GPR waveforms at three different times calculated according to the models indicated by black crosses in Fig. 5 and the true model. The length of the infiltration event is indicated by the light green background.

Fig. 8 Snapshots of the normalized GPR wavefields at a depth of 0.2 m simulated at 12 ns for the GPR measurement conducted at 210 min, based on the (a) true model and (b, c) two selected models indicated by black crosses in Fig. 5. (d, e) Residual wavefields showing the difference with the true model. The layer boundary is shown by the black dashed line. The positions of the transmitter and receiver antenna are indicated by the black circle and black cross, respectively.

Fig. 9 Coupled inversion results from (a) noisy travel times and (b) noisy GPR waveforms. The length of the infiltration event is indicated by the light blue background.

Fig. 10 Water retention $\theta(h)$ and relative hydraulic conductivity $K_r(h)$ functions for the first (a, b) and (c, d) second soil layer obtained from the true model (black line) and 50 possible inverted hydraulic parameters sets from coupled inversion of travel times (yellow dashed lines) and CFWI (purple dashed lines), respectively.

Table 1

Soil hydraulic parameters and layer thicknesses (h_t) used in the synthetic modelling study

	h_t	θ_r	θ_s	α	n	K_s	l
	(m)	($cm^3\ cm^{-3}$)		(cm^{-1})	(-)	(cm min^{-1})	(-)
First layer	0.3	0.043	0.326	0.036	1.386	0.057	1.47
Second layer	1.2	0.053	0.229	0.050	1.534	0.04	-2.78

Table 2

Inverted model parameters for noisy travel time and waveform data

	True value	Bounds	Inverted results	
			Travel times	Waveforms
		2-layer soil profile		
θ_{s1} (cm^3cm^{-3})	0.326	0.30 – 0.40	0.330±0.007	0.326±2.58×10^{-5}†
α_1 (cm^{-1})	0.036	0.030 – 0.125	0.042± 0.017	0.037±0.0002
n_1 (-)	1.386	1.1 – 2.8	1.240±0.125	1.369±0.002
log(K_{s1}) (cm min^{-1})	-1.244	-1.456 – -0.276	-0.976± 0.180	-1.214±0.004
θ_{s2} (cm^3cm^{-3})	0.229	0.15 – 0.30	0.232± 0.007	0.229±4.03×10^{-5}
α_2 (cm^{-1})	0.050	0.030 – 0.125	0.063±0.014	0.049±0.0002
n_2 (-)	1.534	1.1 – 2.8	1.379±0.076	1.527±0.0012
log(K_{s2}) (cm min^{-1})	-1.398	-1.456 – -0.276	-1.123±0.194	-1.396±0.0026
h_t (m)	0.3	0.2 – 0.4	0.29± 0.020	0.30±2.34×10^{-5}
Cost-function	-	-	0.01 (ns)	0.03 (V m^{-1})

†The values indicated the 99% confidence interval based on first-order approximation.

Table 3

Correlation matrix of the inverted hydraulic parameters from CFWI

	α_1 (cm^{-1})	n_1 (-)	$\log(K_{s1})$ (cm min^{-1})	α_2 (cm^{-1})	n_2 (-)	$\log(K_{s2})$ (cm min^{-1})	θ_{s1} (cm^3cm^{-3})	θ_{s2} (cm^3cm^{-3})	h_t (m)
n_1	-0.499	1							
$\log(K_{s1})$	0.488	-0.936†	1						
α_2	-0.228	0.441	-0.424	1					
n_2	0.128	0.474	-0.415	-0.054	1				
$\log(K_{s2})$	-0.248	-0.100	0.042	0.519	-0.783†	1			
θ_{s1}	0.272	-0.417	0.594	-0.054	-0.212	0.049	1		
θ_{s2}	-0.162	-0.010	-0.066	0.259	-0.354	0.474	-0.257	1	
h_t	0.127	-0.105	0.154	-0.043	-0.086	0.067	-0.188	-0.122	1

†The values indicated the pairs of parameters showing strong correlation.

Yi Yu: Conceptualization; Methodology; Writing - Original Draft.

Johan Alexander Huisman: Conceptualization; Methodology; Writing - Review & Editing.

Anja Klotzsche: Methodology.

Harry Vereecken: Supervision; Project administration; Funding acquisition.

Lutz Weihermüller: Conceptualization; Methodology; Writing - Review & Editing.